

See discussions, stats, and author profiles for this publication at: <https://www.researchgate.net/publication/26708057>

Photoinitiated Charge Transport through π -Stacked Electron Conduits in Supramolecular Ordered Assemblies of Donor–Acceptor Triads

ARTICLE *in* JOURNAL OF THE AMERICAN CHEMICAL SOCIETY · AUGUST 2009

Impact Factor: 12.11 · DOI: 10.1021/ja903903q · Source: PubMed

CITATIONS

60

READS

51

5 AUTHORS, INCLUDING:



Raanan Carmielli

Weizmann Institute of Science

44 PUBLICATIONS 866 CITATIONS

[SEE PROFILE](#)

Photoinitiated Charge Transport through π -Stacked Electron Conduits in Supramolecular Ordered Assemblies of Donor–Acceptor Triads

Joseph E. Bullock, Raanan Carmieli, Sarah M. Mickley, Josh Vura-Weis, and Michael R. Wasielewski*

Department of Chemistry and Argonne-Northwestern Solar Energy Research (ANSER) Center,
Northwestern University, Evanston, Illinois 60208-3113

Received May 13, 2009; E-mail: m-wasielewski@northwestern.edu

Abstract: Photochemical electron donor–acceptor triads having an aminopyrene primary donor (APy) and a *p*-diaminobenzene secondary donor (DAB) attached to either one or both imide nitrogen atoms of a perylene-3,4:9,10-bis(dicarboximide) (PDI) electron acceptor were prepared to give DAB-APy-PDI and DAB-APy-PDI-APy-DAB. In toluene, both triads are monomeric, but in methylcyclohexane, they self-assemble into ordered helical heptamers and hexamers, respectively, in which the PDI molecules are π -stacked in a columnar fashion, as evidenced by small- and wide-angle X-ray scattering. Photoexcitation of these supramolecular assemblies results in rapid formation of DAB $^{+*}$ –PDI $^{-*}$ spin-polarized radical ion pairs having spin–spin dipolar interactions, which show that the average distance between the two radical ions is much larger in the assemblies (31 Å) than it is in their monomeric building blocks (23 Å). This work demonstrates that electron hopping through the π -stacked PDI molecules is fast enough to compete effectively with charge recombination (40 ns) in these systems, making these materials of interest as photoactive assemblies for artificial photosynthesis and organic photovoltaics.

Introduction

Achieving functional molecular devices for either solar fuels or electricity production requires hierarchical organization at the supramolecular level similar to that of natural photosynthesis.^{1–3} The design and synthesis of complex, covalent molecular systems comprised of chromophores, electron donors, and electron acceptors, which mimic both the light-harvesting and the charge separation functions of photosynthetic proteins, has been demonstrated.^{4–10} As is the case in photosynthetic reaction center proteins, multicomponent donor–acceptor arrays that carry out multistep charge separation reactions have proven most useful for producing long-lived charge-separated states. Covalent synthesis of functional building blocks with well-defined molecular geometries and donor–acceptor distances

allows precise control over the initial light harvesting and electron transfer events, while self-assembly, or supramolecular organization provides a facile mechanism for assembling large numbers of molecules into structures that can bridge length scales from nanometers to macroscopic dimensions for efficient long distance charge transport. It can also lead to synergistic and emergent properties that are not intrinsic to the building blocks themselves.

Soluble conjugated organic polymers^{11–13} and small molecules^{14–20} have been studied extensively as photoactive materials for solar cells. Unlike most inorganic materials, organic materials allow for solution processing, offering the potential

- (1) Deisenhofer, J.; Epp, O.; Miki, K.; Huber, R.; Michel, H. *J. Mol. Biol.* **1984**, *180*, 385–398.
- (2) Ferreira, K. N.; Iverson, T. M.; Maghlaoui, K.; Barber, J.; Iwata, S. *Science* **2004**, *303*, 1831–1838.
- (3) McDermott, G.; Prince, S. M.; Freer, A. A.; Hawthornthwaite-Lawless, A. M.; Papiz, M. Z.; Cogdell, R. J.; Isaacs, N. W. *Nature* **1995**, *374*, 517–521.
- (4) Wasielewski, M. R. *Chem. Rev.* **1992**, *92*, 435–461.
- (5) Gust, D.; Moore, T. A.; Moore, A. L. *Acc. Chem. Res.* **2001**, *34*, 40–48.
- (6) Holten, D.; Bocian, D. F.; Lindsey, J. S. *Acc. Chem. Res.* **2002**, *35*, 57–69.
- (7) Redmore, N. P.; Rubtsov, I. V.; Therien, M. J. *J. Am. Chem. Soc.* **2003**, *125*, 8769–8778.
- (8) Guldi, D. M. *J. Phys. Chem. B* **2005**, *109*, 11432–11441.
- (9) Martin, N.; Sanchez, L.; Herranz, M. A.; Illescas, B.; Guldi, D. M. *Acc. Chem. Res.* **2007**, *40*, 1015–1024.
- (10) Moore, G. F.; Hambourger, M.; Gervaldo, M.; Poluektov, O. G.; Rajh, T.; Gust, D.; Moore, T. A.; Moore, A. L. *J. Am. Chem. Soc.* **2008**, *130*, 10466–10467.
- (11) Halls, J. M.; Walsh, C. A.; Greenham, N. C.; Marseglia, E. A.; Friend, R. H.; Moratti, S. C.; Holmes, A. B. *Nature* **1995**, *376*, 498–500.
- (12) Yu, G.; Gao, J.; Hummelen, J. C.; Wudl, F.; Heeger, A. J. *Science (Washington, DC, U.S.)* **1995**, *270*, 1789–1791.
- (13) Zhan, X.; Tan, Z.; Domercq, B.; An, Z.; Zhang, X.; Barlow, S.; Li, Y.; Zhu, D.; Kippelen, B.; Marder, S. R. *J. Am. Chem. Soc.* **2007**, *129*, 7246–7247.
- (14) Debije, M. G.; Chen, Z.; Piris, J.; Neder, R. B.; Watson, M. M.; Muellen, K.; Wuerthner, F. *J. Mater. Chem.* **2005**, *15*, 1270–1276.
- (15) Chen, Z.; Stepanenko, V.; Dehm, V.; Prins, P.; Siebbeles, L. D. A.; Seibt, J.; Marquetand, P.; Engel, V.; Würthner, F. *Chem.–Eur. J.* **2007**, *13*, 436–449.
- (16) Dehm, V.; Chen, Z.; Baumeister, U.; Prins, P.; Siebbeles, L. D. A.; Wuerthner, F. *Org. Lett.* **2007**, *9*, 1085–1088.
- (17) Anthony, J. E. *Angew. Chem., Int. Ed.* **2008**, *47*, 452–483.
- (18) An, Z.; Yu, J.; Jones, S. C.; Barlow, S.; Yoo, S.; Domercq, B.; Prins, P.; Siebbeles, L. D. A.; Kippelen, B.; Marder, S. R. *Adv. Mater. (Weinheim, Ger.)* **2005**, *17*, 2580–2583.
- (19) Jones, B. A.; Faccetti, A.; Marks, T. J.; Wasielewski, M. R. *Chem. Mater.* **2007**, *19*, 2703–2705.
- (20) Jones, B. A.; Faccetti, A.; Wasielewski, M. R.; Marks, T. J. *J. Am. Chem. Soc.* **2007**, *129*, 15259–15278.

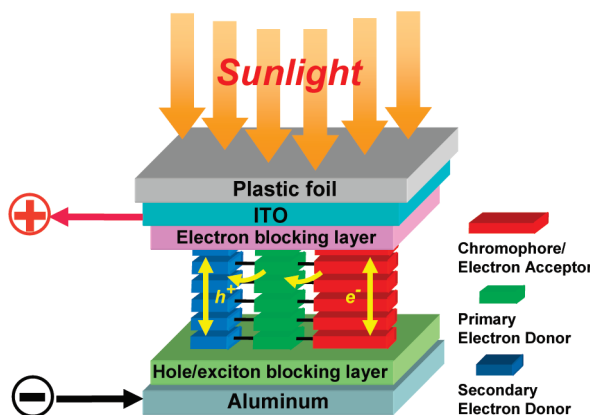


Figure 1. A multilayer organic solar cell in which covalent donor–acceptor building blocks are self-assembled to facilitate charge migration to the electrodes.

of inexpensive device fabrication. However, conjugated polymers have low charge-carrier mobilities relative to those of crystalline aromatic small molecules.¹⁷ This is attributed primarily to poor solid-state order in polymers resulting in charge traps.²¹ Since increasing the degree of order in the solid state most often translates into improved charge carrier mobilities, the use of self-assembly strategies offers the possibility of greatly increasing mobilities in organic materials, while maintaining processing advantages. A conceptual model for a functional organic material for use in a solar cell having efficient photodriven charge separation and subsequent charge transport is depicted in Figure 1. In this model, efficient photodriven multistep charge separation occurs within a covalently linked, donor–acceptor building block resulting in formation of a long-lived radical ion pair (RP, electron–hole pair). Efficient transport of the separated charges over tens of nanometers to the electrodes requires that the RP lifetime is sufficiently long to permit rapid charge hopping of the weakly interacting, uncorrelated charges within self-ordered, segregated, donor and acceptor conduits.

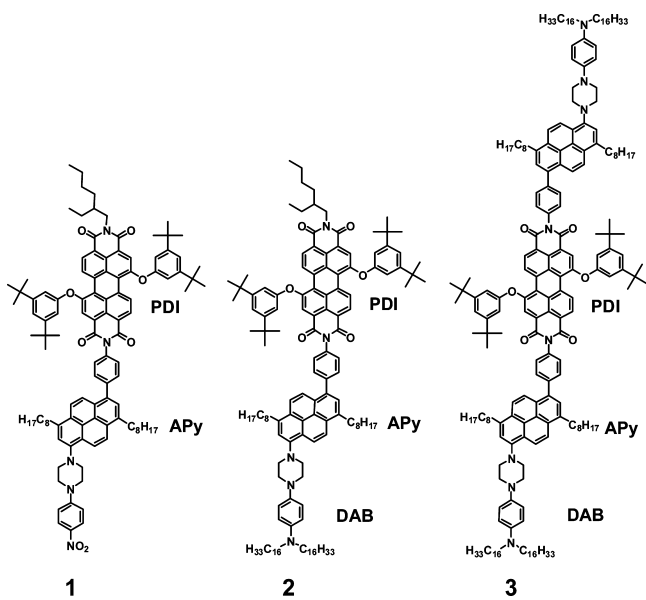
Perylene-3,4:9,10-bis(dicarboximide) (PDI) and its derivatives have attracted significant interest as active materials for light harvesting,^{22–25} photovoltaics,^{26–31} and studies of basic photo-

toinduced charge and energy transfer processes.^{32–34} PDI is both photochemically and thermally stable,³⁵ and can be easily modified at its imide nitrogens, and its 1, 6, 7, and 12 positions. Modifications at these positions tune the electronic properties of PDI resulting in derivatives that absorb light from the near-ultraviolet to the near-infrared region of the spectrum. Moreover, the redox potentials of PDI can be tuned by appropriate substituents resulting in derivatives that are either good electron acceptors³⁶ or donors.³⁷ PDI also demonstrates the ability to self-assemble in solution via hydrophobic/hydrophilic interactions as well as by π – π stacking.^{38–42} Self-assembled, π -stacked PDI systems have been studied extensively; these systems include 1-D assemblies of PDI with a solubilizing group consisting of long alkyl chains at the imide position,⁴³ tethered, extended PDI systems,^{13,16,41,44–48} tetra-substituted phenoxy PDI,^{49,50} bis-1,7-(3',5'-di-*t*-butylphenoxy)-PDI,^{38,51,52} and controlled assemblies of PDI dimers.^{53,54} Many of these systems form *H*-aggregates having nearly cofacial orientations, which promotes enhanced electronic communication between adjacent chromophores enabling efficient energy and/or charge transport.

Recently, we and others have shown that photoinduced charge separation occurs readily in both covalent and self-assembled systems based on robust PDI molecules.^{40,51,54–59} For example,

- (32) Würthner, F.; Thalacker, C.; Sautter, A. *Adv. Mater.* **1999**, *11*, 754–758.
- (33) Langhals, H.; Saulich, S. *Chem.–Eur. J.* **2002**, *8*, 5630–5643.
- (34) Schenning, A. P. H. J.; van Herrikhuyzen, J.; Jonkheijm, P.; Chen, Z.; Würthner, F.; Meijer, E. W. *J. Am. Chem. Soc.* **2002**, *124*, 10252–10253.
- (35) Langhals, H.; Ismael, R. *Eur. J. Org. Chem.* **1998**, *191*, 5–1917.
- (36) Ahrens, M. J.; Fuller, M. J.; Wasielewski, M. R. *Chem. Mater.* **2003**, *15*, 2684–2686.
- (37) Zhao, Y.; Wasielewski, M. R. *Tetrahedron Lett.* **1999**, *40*, 7047–7050.
- (38) Ahrens, M. J.; Sinks, L. E.; Rybtchinski, B.; Liu, W. H.; Jones, B. A.; Giaimo, J. M.; Gusev, A. V.; Goshe, A. J.; Tiede, D. M.; Wasielewski, M. R. *J. Am. Chem. Soc.* **2004**, *126*, 8284–8294.
- (39) Thalacker, C.; Würthner, F. *Adv. Funct. Mater.* **2002**, *12*, 209–218.
- (40) van der Boom, T.; Hayes, R. T.; Zhao, Y. Y.; Bushard, P. J.; Weiss, E. A.; Wasielewski, M. R. *J. Am. Chem. Soc.* **2002**, *124*, 9582–9590.
- (41) Wang, W.; Li, L. S.; Helms, G.; Zhou, H. H.; Li, A. D. Q. *J. Am. Chem. Soc.* **2003**, *125*, 1120–1121.
- (42) Würthner, F. *Chem. Commun.* **2004**, 64–1579.
- (43) Yan, P.; Chowdhury, A.; Holman, M. W.; Adams, D. M. *J. Phys. Chem. B* **2005**, *109*, 724–730.
- (44) Han, J. J.; Wang, W.; Li, A. D. Q. *J. Am. Chem. Soc.* **2006**, *128*, 672–673.
- (45) Neuteboom, E. E.; Meskers, S. C. J.; Meijer, E. W.; Janssen, R. A. J. *Macromol. Chem. Phys.* **2004**, *205*, 217–222.
- (46) Datar, A.; Oitker, R.; Zang, L. *Chem. Commun.* **2006**, 1649–1651.
- (47) Che, Y.; Datar, A.; Balakrishnan, K.; Zang, L. *J. Am. Chem. Soc.* **2007**, *129*, 7234–7235.
- (48) Yagai, S.; Monna, Y.; Kawauchi, N.; Karatsu, T.; Kitamura, A. *Org. Lett.* **2007**, *9*, 1137–1140.
- (49) Kaiser, T. E.; Wang, H.; Stepanenko, V.; Würthner, F. *Angew. Chem., Int. Ed.* **2007**, *46*, 5541–5544.
- (50) Chen, Z.; Baumeister, U.; Tschiesske, C.; Würthner, F. *Chem.–Eur. J.* **2007**, *13*, 450–465.
- (51) Li, X. Y.; Sinks, L. E.; Rybtchinski, B.; Wasielewski, M. R. *J. Am. Chem. Soc.* **2004**, *126*, 10810–10811.
- (52) Zhang, J.; Hoeben, F. J. M.; Pouderoijen, M. J.; Schenning, A. P. H.; Meijer, E. W.; Schryver, F. C.; De Feyter, S. *Chem.–Eur. J.* **2006**, *12*, 9046–9055.
- (53) Rybtchinski, B.; Sinks, L. E.; Wasielewski, M. R. *J. Phys. Chem. A* **2004**, *108*, 7497–7505.
- (54) Rybtchinski, B.; Sinks, L. E.; Wasielewski, M. R. *J. Am. Chem. Soc.* **2004**, *126*, 12268–12269.
- (55) Giaimo, J. M.; Gusev, A. V.; Wasielewski, M. R. *J. Am. Chem. Soc.* **2002**, *124*, 8530–8531.
- (56) You, C.-C.; Würthner, F. *Org. Lett.* **2004**, *6*, 2401–2404.
- (57) Wasielewski, M. R. *J. Org. Chem.* **2006**, *71*, 5051–5066.
- (58) Ahrens, M. J.; Kelley, R. F.; Dance, Z. E. X.; Wasielewski, M. R. *Phys. Chem. Chem. Phys.* **2007**, *9*, 1469–1478.

to address the question of whether unpaired electrons are delocalized or hopping among the PDI derivatives in self-assembled PDI arrays, we have carried out room-temperature, solution-phase EPR and ENDOR studies on the radical anion of a covalent PDI₃ trefoil molecule, which self-assembles into π -stacked dimers.⁶⁰ We have also explored a bichromophoric electron donor–acceptor molecule composed of a zinc tetraphenylporphyrin (ZnTPP) donor surrounded by four perylene-3,4:9,10-bis(dicarboximide) (PDI) acceptors (ZnTPP-PDI₄).⁵⁸ In toluene, ZnTPP-PDI₄ self-assembles into nearly monodisperse aggregates comprised of five molecules arranged in a columnar stack, (ZnTPP-PDI₄)₅. Data for this self-assembled system was compared with that for a monomeric ZnTPP-PDI reference molecule. Femtosecond transient absorption spectroscopy shows that laser excitation of both ZnTPP-PDI and (ZnTPP-PDI₄)₅ results in quantitative formation of ZnTPP⁺–PDI[·] in a few picoseconds. The transient absorption spectra of (ZnTPP-PDI₄)₅ also show that the PDI[·] radical interacts strongly with adjacent PDI molecules and suggests that the electron migrates within the columnar stack. While charge recombination occurs more slowly within (ZnTPP-PDI₄)₅ ($\tau_{\text{CR}} = 4.8$ ns) than it does in the monomeric ZnTPP-PDI reference molecule ($\tau_{\text{CR}} = 3.0$ ns), the ZnTPP⁺–PDI[·] lifetime within the (ZnTPP-PDI₄)₅ assembly is too short for charge transport over long distances through the noncovalent π -stacked molecules to be competitive with charge recombination. In the work described here, we demonstrate that extending the lifetime of the charge separation using two-step electron transfer in covalently linked donor–acceptor triad building blocks **2** and **3** results in fully competitive charge hopping within self-assembled hexamers and heptamers of the triads, thereby demonstrating that the concept illustrated in Figure 1 can be fulfilled in an ordered supramolecular material.



Experimental Section

The syntheses of molecules **1**–**3** are detailed in the Supporting Information.

UV–Vis Spectroscopy and Electrochemistry. Toluene (Aldrich) and nonstabilized HPLC grade dichloromethane (DCM)

(Fisher) were dried using a Glass Contour solvent system, while MCH (Aldrich) was dried over 3 Å molecular sieves. Steady-state absorption spectra were obtained at room temperature on a Shimadzu 1601 UV-vis spectrometer. Electrochemical measurements were performed using a CH Instruments Model 622 electrochemical workstation. All measurements were performed in DCM containing 0.1 M tetra-*n*-butylammonium hexafluorophosphate (TBAPF₆) electrolyte. A 1.0 mm diameter platinum disk electrode, platinum wire counter electrode, and Ag/Ag₂O reference electrode were employed. The ferrocene/ferrocenium redox couple (Fc/Fc⁺, 0.46 vs SCE)⁶¹ was used as an internal reference for all measurements. TBAPF₆ was purchased from Aldrich and recrystallized twice from ethyl acetate prior to use.

Transient Optical Absorption Spectroscopy. Femtosecond transient absorption measurements were made using a regeneratively amplified titanium sapphire laser system operating at a 2 kHz repetition rate.⁵³ The frequency-doubled output of the amplifier was used to pump a two-stage optical parametric amplifier to generate 532 nm, 130 fs laser pulses. A small portion of the fundamental was focused onto a sapphire disk to generate the white-light probe, spanning 425–800 nm. Spectral and kinetic data were collected with a CCD array detector and a 6 ns delay track. Samples in toluene and MCH with an absorbance of 0.4–0.8 at the excitation wavelength were irradiated in 2 mm quartz cuvettes with 1 μ J/pulse focused to a 0.5 mm diameter spot. The total instrument response function was 180 fs. Kinetic analysis was performed at several wavelengths using a Levenberg–Marquardt nonlinear least-squares fit to a sum of exponentials convoluted with a Gaussian instrument response function.

Samples for nanosecond transient absorption spectroscopy were placed in a 10 mm path length quartz cuvette equipped with a vacuum adapter and subjected to four freeze–pump–thaw degassing cycles. The samples were excited with 7 ns, 2 mJ, 532 nm laser pulses generated using the frequency-doubled output of a Continuum Precision II 8000 Nd:YAG laser. The probe light in the nanosecond experiment was generated using a xenon flashlamp (EG&G Electrooptics FX-200) and detected using a photomultiplier tube with high voltage applied to only four dynodes (Hamamatsu R928). The total IRF is 7 ns and is determined primarily by the laser pulse duration.

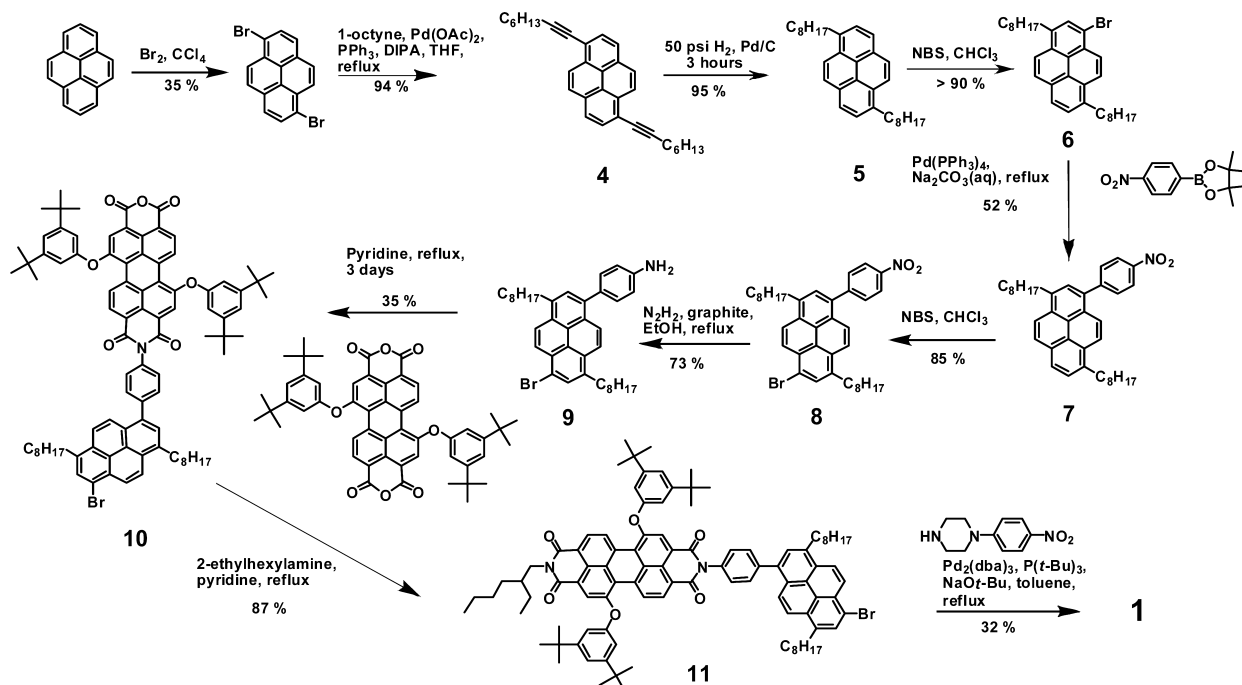
X-ray Scattering. Solutions of **2** and **3** (10^{−3}–10^{−4} M) in MCH were loaded into 2 mm quartz capillaries with a wall thickness of 0.2 mm. X-ray measurements on **2** were carried out at beamline 12-ID-C at the Advanced Photon Source (APS), Argonne National Laboratory. The X-ray scattering instrument utilized a double-crystal Si(111) monochromator and a two-dimensional mosaic CCD detector. The scattering intensity is a function of the scattering vector, q , which is related to the scattering angle 2 θ by the relation $q = (4\pi/\lambda)\sin \theta$, where λ is the X-ray wavelength. The X-ray wavelength was set at $\lambda = 1.0$ Å and the sample-to-detector distances were adjusted to record scattering across two different regions of q : 0.006 Å^{−1} < q < 0.2 Å^{−1} and 0.29 Å^{−1} < q < 2.1 Å^{−1}. X-ray scattering measurements on **3** were carried out using the Dupont-Northwestern-Dow 5-ID-D beamline at the APS. Simultaneous small/wide-angle X-ray scattering (SAXS/WAXS) measurements were made using a Roper Scientific simultaneous SAXS/WAXS system.

Time-Resolved EPR (TREPR) Spectroscopy. Samples for TREPR measurements were prepared by loading a 0.1 mM solution of **2** or **3** into 3.8 mm o.d. (2.4 mm i.d.) quartz tubes, subjecting them to several freeze–pump–thaw degassing cycles on a vacuum line (10^{−4} Torr), and sealing them using a hydrogen torch. TREPR measurements at 295 K and at 85 K were carried out using Bruker Elexsys E580 spectrometer operating at 9.5 GHz. The temperature was controlled by an Oxford Instruments CF935 continuous flow cryostat using liquid nitrogen. Samples were photoexcited at the indicated temperature inside the EPR cavity with 532 nm, 2.5 mJ/

(59) Bullock, J. E.; Kelley, R. F.; Wasielewski, M. R. *PMSE Prepr.* **2007**, 96, 805–806.

(60) Tauber, M. J.; Kelley, R. F.; Giaimo, J. M.; Rybtchinski, B.; Wasielewski, M. R. *J. Am. Chem. Soc.* **2006**, 128, 1782–1783.

(61) Connelly, N. G.; Geiger, W. E. *Chem. Rev.* **1996**, 96, 877–910.

Scheme 1. The Synthesis of **1** Starting from Pyrene

pulse, 7 ns laser pulses at a 10 Hz repetition rate from the frequency-doubled output of a Nd:YAG laser (QuantaRay DCR-2). The polarization of the laser was set to 54.7° relative to the direction of the static magnetic field to avoid magnetophotoselection effects on the spectra. The field modulation was disabled to achieve a time response of $Q/\pi\nu \approx 30$ ns, where Q is the quality factor of the resonator and ν is the resonant frequency, while microwave signals in emission (e) and/or enhanced absorption (a) were detected in both the real and the imaginary channels (quadrature detection). Sweeping the magnetic field gave 2D spectra versus both time and magnetic field. For each kinetic trace, the signal acquired prior to the laser pulse was subtracted from the data. Kinetic traces recorded at magnetic field values off-resonance were considered background signals, whose average was subtracted from all kinetic traces. The spectra were subsequently phased into a Lorentzian part and a dispersive part, and the former, also known as the imaginary magnetic susceptibility χ'' , is presented. BDPA (α,γ -bis diphenylene- β -phenylallyl) dissolved in a polystyrene film and mounted into 0.8-mm-o.d., thin-walled quartz tubes was used as an internal standard for phase alignment of the EPR spectra. Simulation of the powder-pattern spectra of the spin-polarized RPs⁶² and the triplet states^{63,64} resulting from charge recombination was performed using a home-written MATLAB program⁶⁵ following published procedures.

Results and Discussion

Synthesis. The synthesis of the asymmetrically substituted pyrene used as the primary electron donor (APy) in **1–3** begins with the bromination of pyrene, which produces principally the 1,6-dibromo isomer along some of the 1,8-isomer (Scheme 1).⁶⁶ Separation of the dibromopyrene isomers is achieved by repeated recrystallizations; however, it is more convenient to separate the isomers at a later stage of the synthesis. A 2-fold Sonagashira

reaction with 1-octyne yields the dialkynylated pyrene, **4**, which is catalytically hydrogenated to give **5**. Monobromination of **5** to produce **6** proceeds with high selectivity using slow addition of a chloroform solution of NBS. Suzuki cross-coupling of **6** with 4-nitrophenylboronate pinacol ester gives **7**, which is subsequently brominated with NBS to give **8**. The nitro group of **8** is then reduced with hydrazine in the presence of graphite to yield the corresponding aniline **9**, which is condensed with 1,7-bis(3,5-di-*t*-butylphenoxy)perylene-tetracarboxylic dianhydride⁴⁰ to yield monoimide **10**. Further condensation of **10** with 2-ethylhexylamine yields **11**. Finally, palladium-catalyzed Buchwald-Hartwig coupling of **11** with commercially available 1-(4-nitrophenyl)piperazine gives **1**.

The synthesis of **2** and **3** proceeds from **6** by Buchwald-Hartwig coupling with 1-(4-nitrophenyl)piperazine to give **12**, which is brominated to yield tetrasubstituted pyrene **13** (Scheme 2). Reduction of the nitro group in **13** to the amine with hydrazine in the presence of graphite yields the *p*-diaminobenzene (DAB) moiety, **14**, which is very easily oxidized ($E_{\text{ox}} = 0.23$ V vs SCE, see below), making this molecule prone to degradation by exposure to air and light. Thus, the amine was immediately dialkylated using 1-bromohexadecane to form a stable oil, **15**. Suzuki cross-coupling of **15** with 4-nitrophenylboronate pinacol ester yields nitro compound **16**. Reduction of the nitro compound with hydrazine in the presence of graphite yields the air-sensitive yellow amine **17**. Condensation of **17** with the previously reported *N*-(2-ethylhexyl)-1,7-bis(3,5-di-*t*-butylphenoxy)perylene(3,4:9,10)dicarboximidedicarboxyanhydride⁴⁰ yields **2**, while condensation of **17** with 1,7-bis(3,5-di-*t*-butylphenoxy)perylene(3,4:9,10)tetracarboxylic dianhydride yields **3**.⁴⁰

Electronic Absorption Spectroscopy. The electronic spectra of **1–3** in toluene have a strong absorption band at 546 nm, which is characteristic of the (0,0) band of PDI,⁶⁷ and shows a

(62) Till, U.; Hore, P. J. *Mol. Phys.* **1997**, *90*, 289–296.

(63) Kottis, P.; Lefebvre, R. *J. Chem. Phys.* **1963**, *39*, 393–403.

(64) Wasserman, E.; Snyder, L. C.; Yager, W. A. *J. Chem. Phys.* **1964**, *41*, 1763–1772.

(65) MATLAB;; The MathWorks, Inc.: Natick, MA, 2006.

(66) Suenaga, H.; Nakashima, K.; Mizuno, T.; Takeuchi, M.; Hamachi, I.; Shinkai, S. *J. Chem. Soc., Perkin Trans. I* **1998**, 1263–1268.

(67) Giaimo, J. M.; Lockard, J. V.; Sinks, L. E.; Scott, A. M.; Wilson, T. M.; Wasielewski, M. R. *J. Phys. Chem. A* **2008**, *112*, 2322–2330.

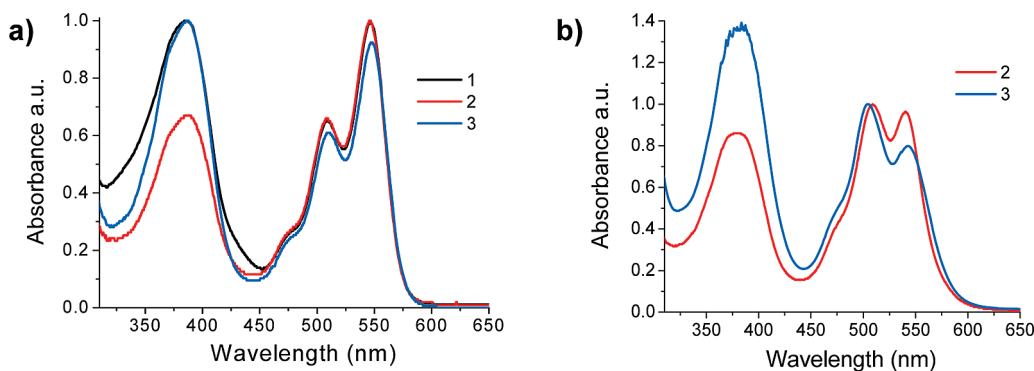
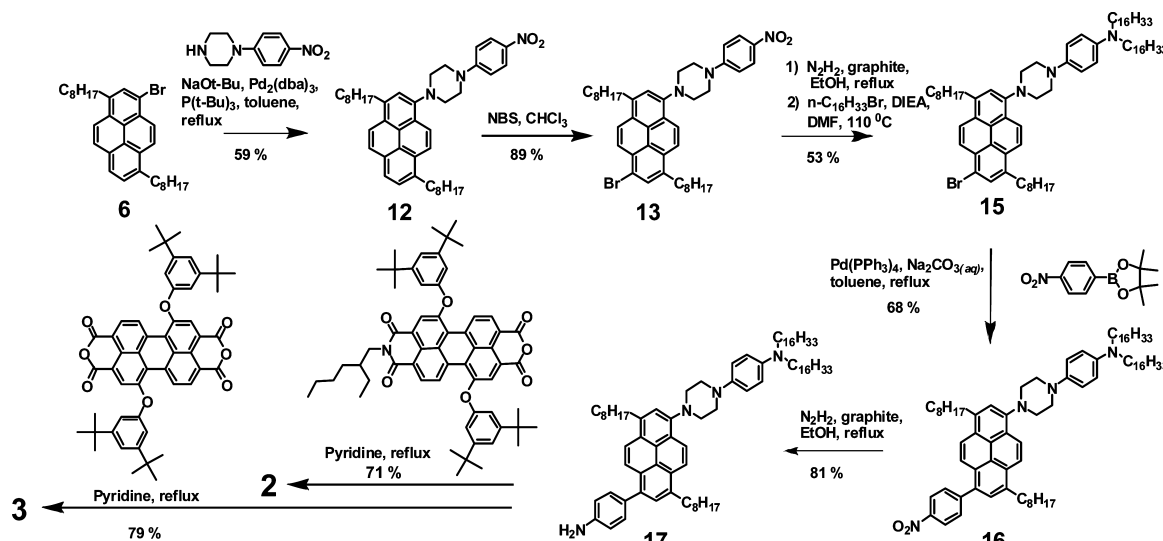


Figure 2. Steady-state absorption for (a) **1**, **2**, and **3** in toluene; and (b) **2** and **3** in methylcyclohexane (MCH).

Scheme 2. Synthesis of Triads **2** and **3**



normal vibronic progression at shorter wavelengths, while the broad, featureless absorption band at 386 nm is typical of substituted pyrenes⁶⁸ (Figure 2a). The pyrene absorption in compound **1** is somewhat more intense than in **2** most likely because the electron withdrawing *p*-nitroaniline group in **1** increases the transition dipole moment through increased conjugation with the electron rich pyrene. The DAB moiety in compounds **2** and **3** also possesses a distinct absorption feature; however, it occurs at shorter wavelengths in the UV region, where it overlaps with absorption features from both APy and PDI.⁶⁹ In contrast, when **2** and **3** are dissolved in methylcyclohexane (MCH), the PDI vibronic bands exhibit distinct intensity changes with the (0,1) band becoming more intense than the (0,0) band. The bands due to pyrene are slightly red-shifted to 380 nm and broadened (Figure 2b). The observed spectral changes of PDI within **2** and **3** are similar to those observed in other PDI-based systems,^{35,41,44,45,70} which form *H*-aggregates and exhibit significant exciton coupling between the π -stacked chromophores. While the spectra indicate that cofacial π -stacking is occurring for both **2** and **3** in MCH, they do not provide

more detailed structural information. Moreover, the proton NMR spectra of **2** and **3** in MCH are severely broadened and do not offer further insights.

Structures of the Supramolecular Assemblies. The Advanced Photon Source at Argonne National Laboratory was used to determine the *solution* structures of the supramolecular assemblies of **2** and **3**. It has been recently demonstrated that small- and wide-angle X-ray scattering (SAXS/WAXS) from monodisperse noncovalent aggregates using a synchrotron source is a powerful tool for the elucidation of their solution-phase structures.^{38,51,54,58–60,71–75} Guinier analysis of the scattering data provides at a minimum the radius of gyration of the complex, R_g , and a gauge of the polydispersity of the aggregates.^{76,77} In favorable cases, if the assemblies are nearly monodisperse, further analysis of the SAXS/WAXS data using

- (68) Kaletas, B. K.; Dobrawa, R.; Sautter, A.; Wuerthner, F.; Zimine, M.; De Cola, L.; Williams, R. M. *J. Phys. Chem. A* **2004**, *108*, 1900–1909.
 (69) Rawashdeh, A. M. M.; Sotiriou-Leventis, C.; Gao, X.; Leventis, N. *Chem. Commun. (Cambridge, U.K.)* **2001**, 1742–1743.
 (70) Hernando, J.; de Witte, P. A. J.; van Dijk, E. M. H. P.; Korterik, J.; Nolte, R. J. M.; Rowan, A. E.; Garcia-Parajo, M. F.; van Hulst, N. F. *Angew. Chem., Int. Ed.* **2004**, *43*, 4045–4049.

- (71) Zhang, R.; Thiagarajan, P.; Tiede, D. M. *J. Appl. Crystallogr.* **2000**, *33*, 565–568.
 (72) Tiede, D. M.; Zhang, R.; Chen, L. X.; Yu, L.; Lindsey, J. S. *J. Am. Chem. Soc.* **2004**, *126*, 14054–14062.
 (73) Kelley, R. F.; Lee, S. J.; Wilson, T. M.; Nakamura, Y.; Tiede, D. M.; Osuka, A.; Hupp, J. T.; Wasielewski, M. R. *J. Am. Chem. Soc.* **2008**, *130*, 4277–4284.
 (74) Kelley, R. F.; Shin, W. S.; Rybtchinski, B.; Sinks, L. E.; Wasielewski, M. R. *J. Am. Chem. Soc.* **2007**, *129*, 3173–3181.
 (75) Kelley, R. F.; Goldsmith, R. H.; Wasielewski, M. R. *J. Am. Chem. Soc.* **2007**, *129*, 6384–6385.
 (76) Guinier, A.; Fournet, G. *Small Angle Scattering*; Wiley: New York, 1955.
 (77) Svergun, D. I.; Koch, M. H. *Rep. Prog. Phys.* **2003**, *66*, 1735–1782.

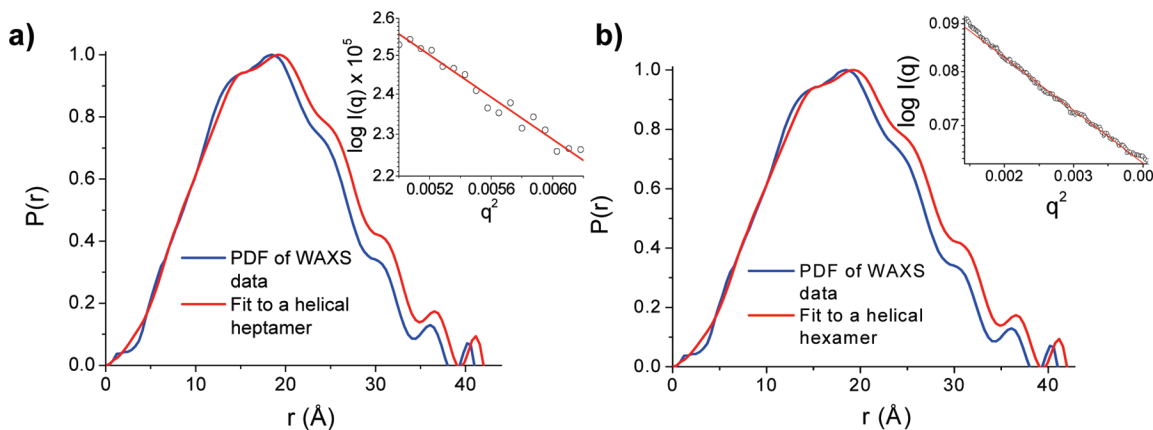


Figure 3. SAXS/WAXS data obtained in MCH. Comparison of pair distribution functions (PDFs) generated from the WAXS data with structural fits to the data for **2** (a) and **3** (b). Insets: Guinier fits using the SAXS data.

atomic pair distance distribution functions (PDFs) and simulated annealing procedures can be performed to obtain the structure in solution with a resolution approaching 3–4 Å for molecular weights up to about 50 kDa.^{77–81} For example, using these techniques, we have previously obtained structures of complex arylene diimide assemblies up to heptamers having a molecular weight of about 28 kDa.^{38,51,53,54} New computational approaches allow SAXS/WAXS data to be interpreted in terms of coordinate models^{71,72,82} and molecular dynamics simulations,^{83,84} and can be used to refine the structures of self-assembled systems.⁸⁵ The ability to carry out structural studies on such assemblies in solution at concentrations typical of time-resolved optical and EPR spectroscopic measurements provides an important connection relating structure to observed function.

The sizes of the assemblies derived from **2** and **3** in solution were determined by analysis of the low q region of the scattering data ($0.006 \text{ \AA}^{-1} < q < 0.2 \text{ \AA}^{-1}$). A plot of the log of the scattering intensity, $I(q)$, versus q^2 over this range of q is linear for both **2** and **3** (Figure 3, insets). According to the Guinier approximation,^{76,86} $I(q) = I(0) \exp(-q^2 R_g^2/3)$, where $I(0)$ is the forward scattering amplitude, and the slope of the linear plot gives the radius of gyration R_g , which is proportional to the size of the assemblies. From the slope of the linear Guinier fits, $R_g = 18.3$ and 19.8 \AA for **2** and **3**, respectively. Structural models of the assemblies based on this information were constructed in Hyperchem⁸⁷ and energy minimized using the MM⁺ force field. PDFs were calculated from the high q experimental scattering data ($0.29 \text{ \AA}^{-1} < q < 2.1 \text{ \AA}^{-1}$) and from the structural models. The structural models were then varied until a best fit with the experimental PDFs for **2** and **3** was found. These best fits are

shown in Figure 3. Both Guinier and PDF analyses yield R_g values which are in excellent agreement with each other. A selection of structural models illustrating the range of structures that were examined are given in the Supporting Information (Figures S1–S4).

Despite the fact that **3** has a larger molecular weight than **2**, their supramolecular assemblies are similar in size, with the data for **2** best fit to a heptamer (**2**₇), while the best fit for **3** yields a hexamer (**3**₆) (Figure 4). The WAXS data did not provide sufficient contrast between the alkyl chains and the solvent, so that they are lost in the subtraction of the solvent scattering. In both structures, the PDI acceptors are approximately 3.4 Å apart and twisted 30° relative to one another. This twisting relieves some of the steric repulsion between the donors and allows the PDI acceptors to π -stack as closely as possible. The structural models show that the helical pitch of the assemblies places the donor ends of the triad monomers at equal spacings along the outer edges of the assemblies. As a result, the DAB donors are positioned ~20 Å apart, rendering charge hopping from DAB⁺ of one triad to DAB of another triad highly unlikely. In contrast, the PDI[–] of one triad is π -stacked in van der Waals contact with the PDIs of neighboring triads in the stacked assembly, so that charge hopping of the unpaired electron from PDI[–] to a neighboring PDI is likely, as we have demonstrated in chemically reduced PDI assemblies.⁶⁰

Charge Separation and Recombination. The energy of the lowest excited singlet state of the monomeric PDI derivative used in **1–3** is 2.23 eV.⁶⁷ However, the absorption spectra of the π -stacked PDI molecules within **2**₇ and **3**₆ in MCH (Figure 2b) exhibit an exciton splitting (2V) of approximately 0.35 eV, so that the electronic absorption of the strongly disallowed lower exciton state of the PDI in the aggregates should occur at about 2.1 eV. Assuming that the Stokes shift of the exciton coupled PDI molecules following excitation is comparable to that of the PDI monomer, the energy of the lower exciton state of the PDI in **2**₇ and **3**₆ is estimated to be about 2.05 eV. The energies of the excimer-like states of the PDI in **2**₇ and **3**₆ should be even lower, since the emission maxima of covalent, cofacial PDI dimers occur at about 695 nm or 1.79 eV.⁶⁷

The one-electron oxidation and reduction potentials for **1–3** are summarized in Table 1. Neither the oxidation potentials of the DAB and APy donors nor the reduction potential of the PDI acceptor used to construct the triads is significantly affected by covalent linkages between the two redox active centers. The energies of DAB-APy⁺-PDI[–] (ΔG_{RPI}) and DAB⁺-APy-PDI[–]

- (78) Petoukhov, M. V.; Eady, N. A. J.; Brown, K. A.; Svergun, D. I. *Biophys. J.* **2002**, *83*, 3113–3125.
- (79) Svergun, D. I. *J. Appl. Crystallogr.* **1992**, *25*, 495–503.
- (80) Svergun, D. I. *Biophys. J.* **1999**, *76*, 2879–2886.
- (81) Volkov, V. V.; Svergun, D. I. *J. Appl. Crystallogr.* **2003**, *36*, 860–864.
- (82) O'Donnell, J. L.; Zuo, X.; Goswami, A. J.; Sarkisov, L.; Snurr, R. Q.; Hupp, J. T.; Tiede, D. M. *J. Am. Chem. Soc.* **2007**, *129*, 1578–1585.
- (83) Zuo, X.; Cui, G.; Mertz, K. M.; Zhang, L.; Lewis, F. D.; Tiede, D. M. *Proc. Natl. Acad. Sci. U.S.A.* **2006**, *103*, 3534–3539.
- (84) Mardis, K. L.; Sutton, H. M.; Zuo, X. B.; Lindsey, J. S.; Tiede, D. M. *J. Phys. Chem. A* **2009**, *113*, 2516–2523.
- (85) Zuo, X.; Wang, J.; Foster, T. R.; Schwieters, C. D.; Tiede, D. M.; Butcher, S. E.; Wang, Y.-X. *J. Am. Chem. Soc.* **2008**, *130*, 3292–3293.
- (86) Glatter, O. *Neutron, X-ray and Light Scattering*; Elsevier: Amsterdam, 1991.
- (87) Hyperchem; Hypercube, Inc.: Gainesville, FL.

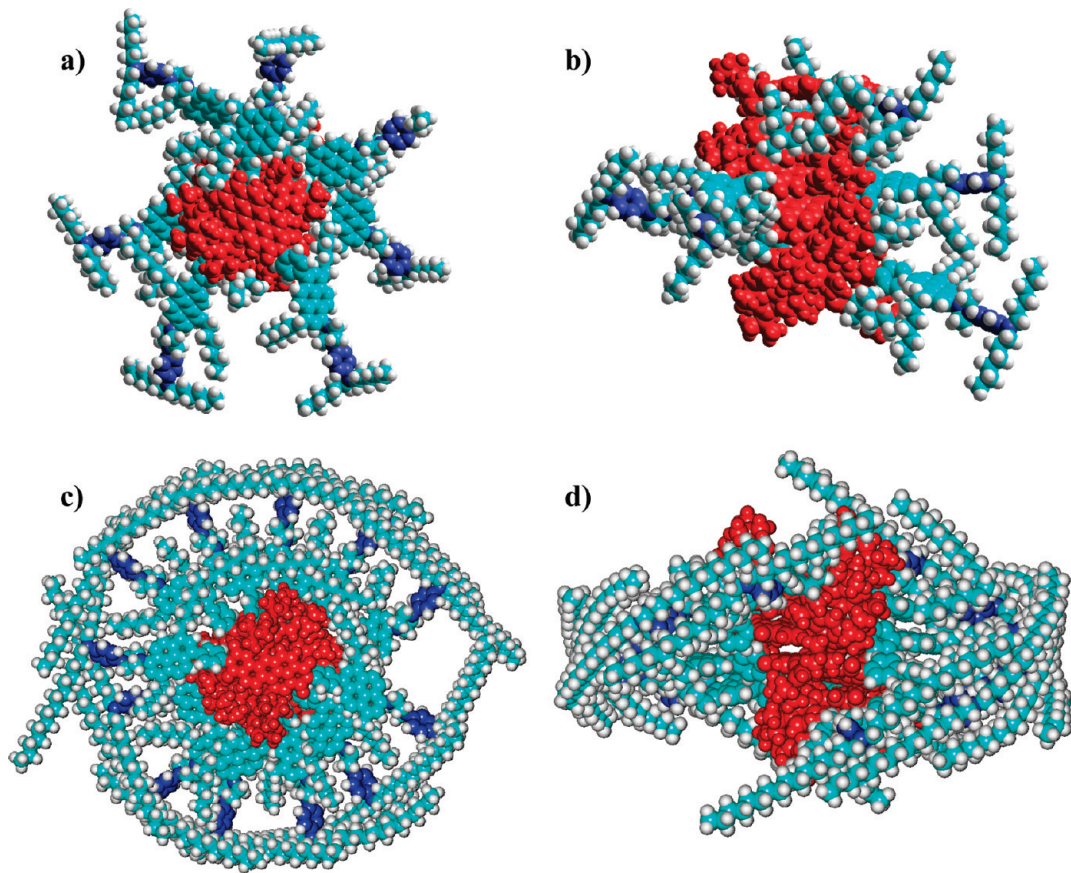


Figure 4. MM⁺ optimized structures that yield the best fits to the experimental SAXS/WAXS data. Structure for **2₇** (a) top view and (b) side view. Structure for **3₆** (c) top view and (d) side view. PDI is red, APy is cyan, and DAB is blue.

Table 1. Redox Potentials vs SCE^a and Radical Ion Pair Energies

comp.	DAB		APy		PDI		toluene		MCH	
	E_{OX1}	E_{OX2}	E_{OX1}	E_{OX2}	E_{RED1}	E_{RED2}	ΔG_{RP1}	ΔG_{RP2}	ΔG_{RP1}	ΔG_{RP2}
1	—	—	1.01	1.25	-0.62	-0.85	1.86	—	1.94	—
2	0.23	0.81	1.03	1.23	-0.61	-0.84	1.87	1.24	1.95	1.36
3	0.22	0.80	1.03	1.23	-0.60	-0.83	1.86	1.23	1.94	1.35

^a Values obtained by differential pulse voltammetry in dry CH₂Cl₂ with 0.1 M Bu₄NPF₆ as the supporting electrolyte and Fc/Fc⁺ as the internal standard.

(ΔG_{RP2}) were calculated using methods described earlier^{88,89} from the experimentally determined redox potentials along with the ionic radii and donor–acceptor distances (see Supporting Information), which were estimated using the MM⁺ energy minimized ground state structures of **2** and **3**.⁸⁷ A comparison of the PDI excited singlet state and RP energies indicates that the two-step electron transfer sequence: DAB-APy-^{1*}PDI → DAB-APy⁺⁻-PDI^{•-} → DAB⁺⁻-APy-PDI^{•-} should occur in monomeric **2** and **3**, and it should also occur from the lower exciton state of ^{1*}PDI in **2₇** and **3₆**, but not from the excimer-like state of PDI, which is too low in energy.

We have used transient absorption spectroscopy to characterize the formation of these RP states. Molecule **1** serves as the dyad reference molecule for triads **2** and **3**. Selective photoexcitation of the PDI chromophore in **1** with 130 fs, 532 nm laser pulses results in the transient absorption spectra shown in Figure 5a. They are characterized at early times by a bleach of the

ground state absorption of PDI and the appearance of a stimulated emission feature at 600 nm as well as a broad absorption feature near 700 nm, which are typical of ^{1*}PDI.⁶⁷ Notably, the 700 nm feature sharpens and red-shifts to 725 nm with $\tau_{CS} = 9.8$ ps, which is indicative of formation of PDI^{•-},^{90,91} as a result of the reaction APy⁺⁻-PDI → APy⁺⁻-PDI^{•-}. Subsequently, APy⁺⁻-PDI^{•-} decays back to ground state with $\tau_{CR} = 1.1$ ns. In contrast, the femtosecond transient absorption spectra of **2** and **2₇** (Figures S5a and S5b, respectively) and **3** and **3₆** (Figure 5, panels b and c, respectively) show that PDI^{•-} appears in a few picoseconds (Table 2) and persists for the entire 6 ns range of available pump–probe delay times. The formation of PDI^{•-} in **2₇** and **3₆** is faster than the formation of the PDI excimer-like state from its lower exciton state for the PDI

(88) Weller, A. Z. *Phys. Chem.* **1982**, *133*, 93–98.

(89) Greenfield, S. R.; Svec, W. A.; Gosztola, D.; Wasielewski, M. R. *J. Am. Chem. Soc.* **1996**, *118*, 6767–6777.

(90) Gosztola, D.; Niemczyk, M. P.; Svec, W. A.; Lukas, A. S.; Wasielewski, M. R. *J. Phys. Chem. A* **2000**, *104*, 6545–6551.

(91) Kelley, R. F.; Tauber, M. J.; Wasielewski, M. R. *J. Am. Chem. Soc.* **2006**, *128*, 4779–4791.

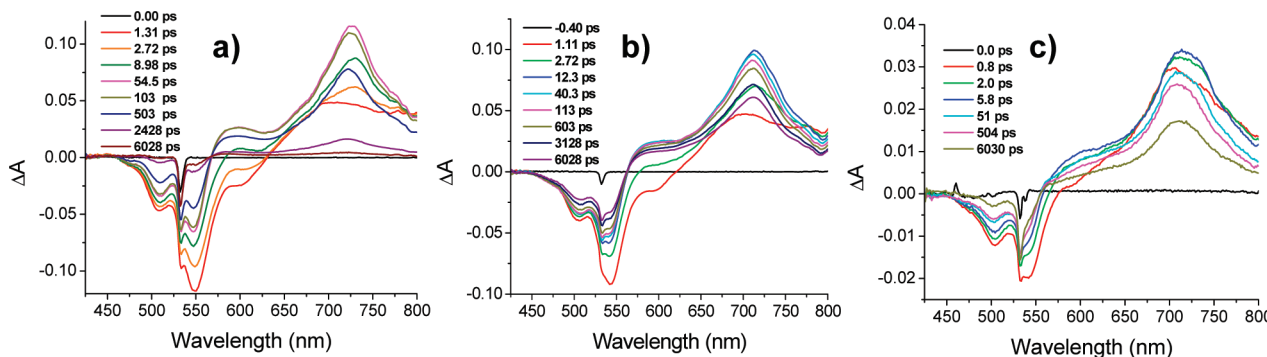


Figure 5. Femtosecond transient absorption spectra for (a) **1** in toluene, (b) **3** in toluene, (c) **3**₆ in MCH following a 130 fs, 532 nm laser pulse.

Table 2. Time Constants for Charge Separation (τ_{CS}) and Recombination (τ_{CR})

compound	τ_{CS} (ps)		τ_{CR} (ns)	
	toluene	MCH	toluene	MCH
1	9.8 ± 0.4	—	1.1 ± 0.1	—
2	6.7 ± 0.3	5.6 ± 0.1	33.4 ± 1.5	49.2 ± 1.2
3	3.2 ± 0.1	1.3 ± 0.1	34.2 ± 0.2	40.0 ± 0.4

geometry found in these assemblies.⁹² The persistence of the transient absorption changes over the 6 ns time window of these experiments results from the rapid secondary electron transfer reaction: DAB-APy⁺-PDI⁻ → DAB⁺-APy-PDI⁻. The observed PDI⁻ absorption band in MCH is somewhat broader than that observed in toluene. The extinction coefficient of DAB⁺ is about 4.5 times smaller than that of PDI⁻,⁹³ so that the spectral changes expected for DAB⁺ formation are overwhelmed by the larger changes due to the PDI ground state bleach. Nanosecond transient absorption spectroscopy was used to determine the lifetime of DAB⁺-APy-PDI⁻ for **2** and **2**₇ (Figures S6a and S6b, respectively) and for **3** and **3**₆ (Figure 6, panels a and b, respectively). The data show that DAB⁺-APy-PDI⁻ recombines on a ∼33–50 ns time scale with significantly longer lifetimes observed for **2**₇ and **3**₆ relative to those of **2** and **3**, respectively. At times longer than about 200 ns, the spectra show small residual absorption changes that are attributed to the formation of DAB-APy-³PDI upon charge recombination (Figure 6, insets). The time constants for the initial photoinduced charge separation and final recombination are given in Table 2.

Radical Pair TREPR Spectra and Charge Separation Distances. TREPR measurements were used to probe the competition between charge recombination and charge transport within the self-assembled, π -stacked structures of **2**₇ and **3**₆. Following rapid, two-step charge separation, the initially formed singlet RP, ¹(DAB⁺-APy-PDI⁻), undergoes radical-pair inter-system crossing (RP-ISC)^{94,95} to produce the triplet RP, ³(DAB⁺-APy-PDI⁻). TREPR measurements were carried out in a 350 mT magnetic field, so that the triplet sublevels of ³(DAB⁺-APy-PDI⁻) undergo Zeeman splitting, and are best described by the T₊₁, T₀, and T₋₁ eigenstates that are quantized

along the applied magnetic field. RP-ISC depends on both the spin–spin exchange interaction, 2J, and the dipolar interaction, D, between the two radicals that comprise the RP. The magnitude of 2J depends exponentially on the distance *r* between the two radicals and is assumed to be isotropic, while that of D depends on 1/r³ and is anisotropic. For large molecules in solution, such as supramolecular assemblies **2**₇ and **3**₆, and for molecules in the solid state, D is not rotationally averaged to zero. D is usually approximated by the point dipole model,⁹⁶

$$D = -\frac{3\mu_0 g_e^2 \beta_e^2}{8\pi r^3} \quad (1)$$

where μ_0 , g_e , and β_e are the vacuum permeability, electronic g-factor and Bohr magneton, respectively. In units of mT and Å, $D = -2785 \text{ mT}\cdot\text{\AA}/r^3$. When RP distances are >~10–15 Å, both D and 2J are small, so that the S and T₀ spin states of the RP are close in energy and mix, while the T₊₁ and T₋₁ states are energetically far removed from T₀ and do not mix with S.^{97,98} The two RP states that result from S-T₀ mixing are preferentially populated due to the initial population of S, so that the four $\Delta m = \pm 1$ EPR transitions that occur between these two mixed states and T₊₁ and T₋₁ display an intensity pattern characteristic of the strong spin polarization.^{94,95} The TREPR spectrum consists of two antiphase doublets, centered at the g-factors of the individual radicals that comprise the pair, in which the splitting of each doublet is determined by 2J and D. The electron spin polarization pattern of the EPR signal, that is, which transitions are in enhanced absorption (*a*) or emission (*e*), low field to high field, is determined by the sign rule,^{98,99}

$$\Gamma = \mu \cdot \text{sign}[J - D(3 \cos^2(\xi) - 1)] = \begin{cases} (-) \text{ gives } e/a \\ (+) \text{ gives } a/e \end{cases} \quad (2)$$

where ξ is the angle between the dipolar axis of the radical pair and the direction of the magnetic field B_0 and μ is -1 or +1 for a singlet or triplet excited state precursor, respectively. Since ultrafast charge separation in **2** and **3** as well as in **2**₇ and **3**₆ proceeds from ¹PDI and the resultant RP spectra exhibit an (*e*, *a*) spin polarization pattern, eq 2 restricts the signs and

- (92) Hariharan, M.; Zheng, Y.; Long, H.; Zeidan, T. A.; Schatz, G. C.; Vura-Weis, J.; Wasielewski, M. R.; Zuo, X.; Tiede, D. M.; Lewis, F. D. *J. Am. Chem. Soc.* **2009**, *131*, 5920–5929.
- (93) Steigman, J.; Cronkright, W. *J. Am. Chem. Soc.* **1970**, *92*, 6736–6743.
- (94) Closs, G. L.; Forbes, M. D. E.; Norris, J. R. *J. Phys. Chem.* **1987**, *91*, 3592–3599.
- (95) Hore, P. J.; Hunter, D. A.; McKie, C. D.; Hoff, A. *J. Chem. Phys. Lett.* **1987**, *137*, 495–500.

- (96) Efimova, O.; Hore, P. J. *Biophys. J.* **2008**, *94*, 1565–1574.
- (97) Kobori, Y.; Yamauchi, S.; Akiyama, K.; Tero-Kubota, S.; Imahori, H.; Fukuzumi, S.; Norris, J. R., Jr. *Proc. Natl. Acad. Sci. U.S.A.* **2005**, *102*, 10017–10022.
- (98) Dance, Z. E. X.; Mi, Q. X.; McCamant, D. W.; Ahrens, M. J.; Ratner, M. A.; Wasielewski, M. R. *J. Phys. Chem. B* **2006**, *110*, 25163–25173.
- (99) Hore, P. J. In *Advanced EPR in Biology and Biochemistry*; Hoff, A. J., Ed.; Elsevier: Amsterdam 1989, pp 405–440.

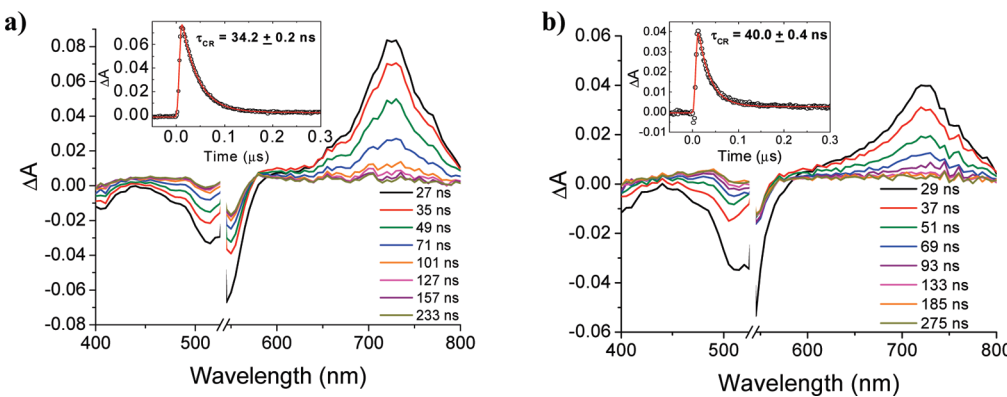


Figure 6. Nanosecond transient absorption spectra for (a) **3** in toluene, (b) **3** in MCH following a 7 ns, 532 laser pulse. Insets: transient absorption kinetics at 725 nm.

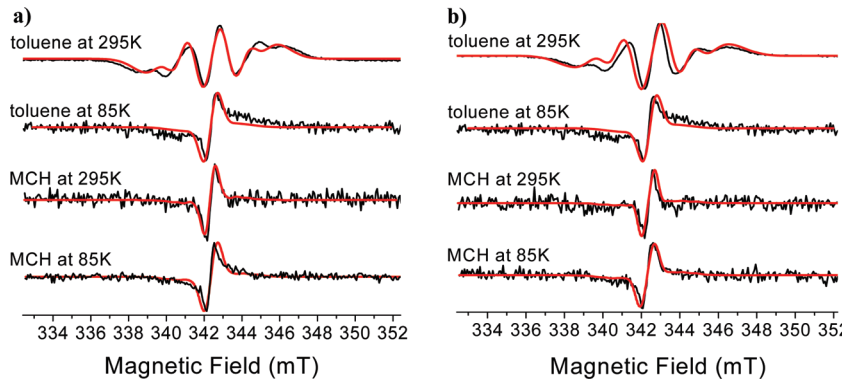


Figure 7. TREPR spectra of **2** (a) and **3** (b) at 85 K and at 100 ns following a 532 nm, 2.5 mJ laser pulse. The smooth curves superimposed on the experimental spectra are computer simulations of the RP spectra using the parameters given in Table 1.

Table 3. RP Simulation Parameters for **2** and **3** at 100 ns after the Laser Pulse

comp.	solvent	T (K)	2J (mT)	D (mT)	r (Å)	$k_{SS} 10^6$ (s ⁻¹)	$k_{TR} 10^6$ (s ⁻¹)
2	TOL	295	2.50 ± 0.01	—	23.2 ^a	31 ± 1	22 ± 1
2	TOL	85	0.20 ± 0.01	-0.08 ± 0.01	32 ± 1	3.0 ± 0.1	6.0 ± 0.1
2 ₇	MCH	295	0.27 ± 0.01	-0.09 ± 0.01	31 ± 1	10 ± 1	16 ± 1
2	MCH	85	0.27 ± 0.01	-0.09 ± 0.01	31 ± 1	4.0 ± 0.1	7.2 ± 0.1
3	TOL	295	2.76 ± 0.01	—	23.2 ^a	32 ± 1	19 ± 1
3	TOL	85	0.32 ± 0.01	-0.10 ± 0.01	30 ± 1	5.0 ± 0.1	13 ± 1
3 ₆	MCH	295	0.30 ± 0.01	-0.09 ± 0.01	31 ± 1	10 ± 1	16 ± 1
3	MCH	85	0.32 ± 0.01	-0.09 ± 0.01	31 ± 1	5.9 ± 0.1	10 ± 1

^a Distances calculated from energy-minimized ground state structures (see text).

magnitudes that $2J$ and D can adopt. Given that D is negative (eq 1), if $2J > 0$, eq 2 predicts an (*e, a*) pattern for all values of $2J$ and D , while if $2J < 0$, eq 2 predicts an (*e, a*) pattern only when $|D(3 \cos^2(\xi) - 1)| > |2J|$.^{94,95}

Photoexcitation of **2** and **3** as well as assemblies **2**₇ and **3**₆ with a 532 nm, 7 ns laser pulse produces spin-polarized RP signals having an (*e, a*) phase pattern at both 295 K and at 85 K (Figure 7). The spectra were simulated with the spin-correlated radical pair (SCRP) model^{62,94,95,100,101} using the reported hyperfine coupling constants for DAB⁺¹⁰² and PDI⁻⁶⁰. The fits to the data are given in Figure 7, and the fitting parameters are summarized in Table 3. On the basis of UV-vis

spectra, NMR, and the SAXS/WAXS results, molecules **2** and **3** are monomeric in toluene at 295 K, but assemble into the helical assemblies **2**₇ and **3**₆, respectively, in MCH. The formation of these large assemblies in MCH is also reflected in a comparison of the TREPR spectra of DAB⁺¹⁰³-APy-PDI⁻ in **2** and **3** (toluene) and in **2**₇ and **3**₆ (MCH) at 295 K. The values of the exchange interaction $2J$ for monomeric **2** and **3** in toluene at 295 K are 2.50 and 2.76 mT, respectively, while those of **2**₇ and **3**₆ decrease to about 0.3 mT. At 85 K, **2** and **3** as well as **2**₇ and **3**₆ show similar RP spectra with $2J \sim 0.2\text{--}0.3$ mT, which is most likely due to the formation of supramolecular assemblies of sizes comparable to **2**₇ and **3**₆ upon freezing. The value of $2J$ depends exponentially on the distance between the two radical ions, so that $2J$ is small when the distance r is large, and can be described by¹⁰³

- (100) Buckley, C. D.; Hunter, D. A.; Hore, P. J.; McLauchlan, K. A. *Chem. Phys. Lett.* **1987**, *135*, 307–312.
- (101) Norris, J. R.; Morris, A. L.; Thurnauer, M. C.; Tang, J. J. *Chem. Phys.* **1990**, *92*, 4239–4249.
- (102) Grampf, G.; Kelteiner, A. M.; Landgraf, S.; Sacher, M.; Niethammer, D.; Telo, J. P.; Dias, R. M. B.; Vieira, A. J. S. C. *Monats. Chem.* **2005**, *136*, 519–536.

- (103) De Kanter, F. J. J.; Kaptein, R.; Van Santen, R. A. *Chem. Phys. Lett.* **1977**, *45*, 575–579.

$$2J = 2J_0 e^{-\alpha(r-r_0)} \quad (3)$$

where $2J_0$ is the spin–spin exchange interaction at van der Waals contact, α is a constant, and r_0 is the van der Waals contact distance of about 3.5 Å. Thus, the decrease in $2J$ upon assembly of **2** and **3** into supramolecular species **2₇** and **3₆** indicates that the average distance between the photogenerated radical ions has increased significantly in **2₇** and **3₆**. However, problems arise when attempts are made to use values of $2J$ and eq 3 as a molecular “ruler” to compare charge separation distances in monomeric **2** and **3** with those in **2₇** and **3₆** because the radical ions within **2** and **3** are separated by covalent bonds, while those in **2₇** and **3₆** are separated by both covalent bonds and noncovalent π – π interactions through a variety of pathways, which results in different effective values of $2J_0$.

A much better gauge of average RP distances in these systems is obtained from the dipolar spin–spin interaction D using the point dipole approximation, eq 1. The D values for monomeric **2** and **3** in toluene at 295 K are averaged to zero by the tumbling motions of these molecules in solution, so that the intramolecular RP distance in DAB⁺-APy-PDI[−] is estimated from the calculated ground state geometry of DAB-APy-PDI using the PM3 method.¹⁰⁴ The spins within DAB⁺ and PDI[−] are symmetrically distributed across their individual π systems, which results in a 23.2 Å DAB⁺-APy-PDI[−] distance. In contrast, the tumbling rates of **2₇** and **3₆** in MCH at 295 K are sufficiently slow that simulations of their TREPR spectra yield D values, which give an average RP distance of 31 Å using eq 1. This average distance is much larger than the 23.2 Å intramolecular DAB⁺-APy-PDI[−] distance and is consistent with charge migration through the π -stacked PDI molecules (Figure 8). The values of D obtained for **2** and **3** in MCH at 85 K are the same as those at 295 K, which suggests that charge hopping is not adversely affected by lowering the temperature. Interestingly, cooling the toluene samples of monomeric **2** and **3** to 85 K also produces RP spectra having the same $2J$ and D values as do **2₇** and **3₆** in MCH. We have no structural information regarding the size of the assemblies that form upon cooling these systems to 85 K; however, the TREPR data suggest that they form supramolecular assemblies in which electron transport occurs among at least 6 or 7 π -stacked PDI molecules.

The values of D clearly show that the average distance between DAB⁺ and PDI[−] within **2₇** and **3₆** increase substantially relative to those in monomeric **2** and **3**. Yet, on a purely statistical basis, assuming equal probabilities for photoexciting each PDI chromophore within **2₇** and **3₆**, as well as for producing each possible DAB⁺-PDI[−] RP within the structure as a result of rapid charge hopping between PDI molecules, the average RP distance based on the structures obtained from the SAXS/WAXS measurements should only increase to 25.2 Å in **2₇** and to 24.0 Å in **3₆** (Table S1). The much longer observed average RP distances within both supramolecular assemblies are due to a distance distribution that favors the longer distances within them, since the maximum RP distance in **2₇** is 35.4 Å, while that in **3₆** is 32.7 Å. For these small assemblies, the data suggests that the electrons are being preferentially trapped at PDI acceptors that are at the ends of the PDI stack. This may be a consequence of the abrupt change in PDI solvation environment at the terminal PDI molecules of the π -stack relative to the solvation environment of the internal PDI molecules within the π -stack.

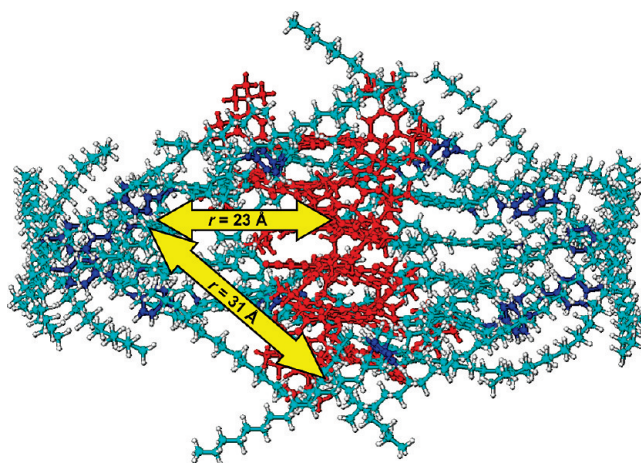


Figure 8. Inter- vs intramolecular charge separation distance for **3** in MCH.

TREPR Spectra of Triplet States Resulting from Charge Recombination. The charge recombination process in **2**, **3**, **2₇**, and **3₆** is spin selective; that is, ¹(DAB⁺-PDI[−]) recombines to the singlet ground state, while ³(DAB⁺-PDI[−]) recombines to yield the triplet ^{3*}PDI, which acquires the non-Boltzmann spin population of the triplet RP state.¹⁰⁵ The spin polarization of the EPR transitions exhibited by ^{3*}PDI can be differentiated from those of a triplet state formed by the ordinary spin-orbit intersystem crossing mechanism by the polarization pattern of its six EPR transitions at the canonical (x , y , z) orientations relative to the applied magnetic field. A RP precursor that undergoes the RP-ISC mechanism by S-T₀ mixing followed by charge recombination uniquely yields an (a , e , e , a , a , e) (low field to high field) polarization pattern.¹⁰⁵

Similar triplet TREPR spectra are observed for **2₇** and **3₆** at both 295 and 85 K (Figure 9), with each having an overall width of ~80 mT and an electron spin polarization pattern (a , e , e , a , a , e) uniquely attributable to a triplet state formed by the RP-ISC mechanism. The narrow RP spectrum that appears at $g \sim 2$ was discussed above. The appearance of fully resolved anisotropic triplet spectra for **2₇** and **3₆** at 295 K can be explained by the slow tumbling rate of these protein-sized assemblies, relative to the frequencies of their zero-field splittings. We recently observed similar phenomena in large rod-like PDI-based donor–acceptor systems.⁹⁸ Even in toluene, where molecules **2** and **3** are in their monomeric form, a weak triplet spectrum appears at 295 K indicating that their tumbling rate is slow enough, so that the zero-field splitting tensor is not completely averaged to zero. The weak triplet observed for **2** and **3** in toluene at 295 K could not be accurately simulated because of its low signal-to-noise. All spectra obtained at 85 K have very similar zero-field splitting parameters D and E of about 40 and 7 mT, respectively (Table 4), while those obtained at 295 K exhibit smaller D values due to a slight narrowing of the spectrum as a result of partial averaging because of molecular tumbling. The appearance of triplet states having transitions with the spin polarization pattern diagnostic for the RP-ISC mechanism, even at room temperature, certifies that the spin–spin interactions D and J within the photogenerated RPs are very weak. Thus, all the observed spin dynamics within these supramolecular assemblies are consistent with long average RP

(104) Stewart, J. J. *P. J. Comput. Chem.* **1989**, *10*, 209–220.

(105) Levanon, H.; Hasharoni, K. *Prog. React. Kinet.* **1995**, *20*, 309–346.

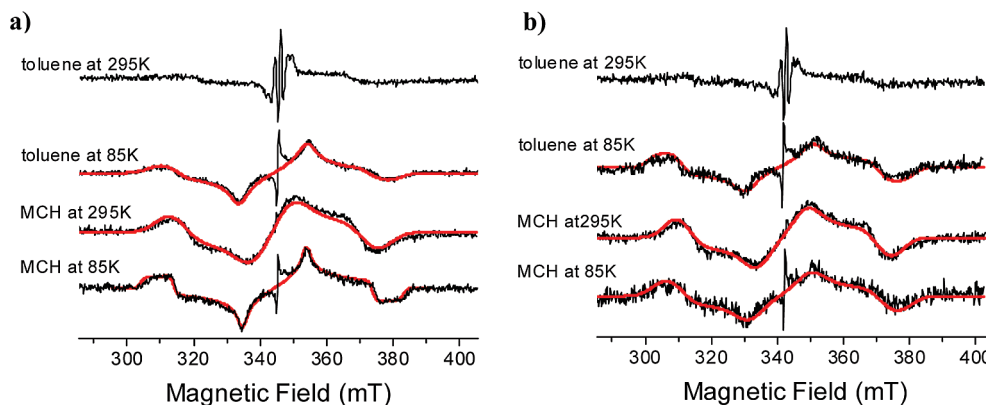


Figure 9. TREPR spectra of **2** (a) and **3** (b) recorded at 85 and at 295 K. The smooth curves superimposed on the experimental spectra are computer simulations of the triplet spectra.

Table 4. Zero Field Splitting Parameters Obtained from Simulations of Triplet State TREPR Spectra

comp.	solvent	T (K)	D (mT)	E (mT)
2	toluene	295	—	—
2	toluene	85	40.5 ± 0.1	6.5 ± 0.1
2	MCH	295	34.0 ± 0.1	7.4 ± 0.1
2	MCH	85	39.6 ± 0.1	6.8 ± 0.1
3	toluene	295	-	-
3	toluene	85	40.4 ± 0.1	6.6 ± 0.1
3	MCH	295	36.3 ± 0.1	7.0 ± 0.1
3	MCH	85	39.7 ± 0.1	7.0 ± 0.1

distances, which, in turn, are indicative of rapid charge transport between the π -stacked PDI molecules.

Conclusions

We have shown that extending the lifetime of photoinitiated charge separation using two-step electron transfer in covalently linked donor–acceptor triad building blocks results in fully competitive charge hopping within self-assembled hexamers and heptamers of the triads, thereby demonstrating that charge transport between noncovalent acceptors can compete effectively with charge recombination within the covalent building blocks. We are currently extending this approach to prepare triad building blocks in which self-assembly will produce ordered

charge transport conduits for both holes and electrons, thus, making these materials of interest as photoactive assemblies for both artificial photosynthesis and organic photovoltaics. The challenge for the future is to develop strategies to template these materials onto electrodes in the appropriate orientation that directs charge transport efficiently from the conduits to the electrodes.

Acknowledgment. This work was supported by the Chemical Sciences, Geosciences, and Biosciences Division, Office of Basic Energy Sciences, DOE under grant no. DE-FG02-99ER14999. Portions of this work were performed at the Dupont-Northwestern-Dow Collaborative Access Team (DND-CAT) located at Sector 5 of the Advanced Photon Source (APS). DND-CAT is supported by E.I. DuPont de Nemours & Co., The Dow Chemical Company and the State of Illinois. Use of the APS was supported by the U.S. Department of Energy, Office of Science, Office of Basic Energy Sciences, under Contract No. DE-AC02-06CH11357.

Supporting Information Available: Experimental details including synthesis, additional SAXS/WAXS data, structural models, and transient absorption data. This material is available free of charge via the Internet at <http://pubs.acs.org>.

JA903903Q